atmosphere

MDPI

Article

Decadal Variability of the Lagged IOD–ENSO Relationship in CMIP6 Models

Hualong Zhu *, Yutong Zhang, Kaijie Duan and Jiaqing Xue

Collaborative Innovation Center on Forecast and Evaluation of Meteorological Disasters (CIC-FEMD), Key Laboratory of Meteorological Disaster of Ministry of Education, International Joint Laboratory on Climate and Environment Change (ILCEC), Nanjing University of Information Science and Technology, Nanjing 210044, China
* Correspondence: zhuhualong@nuist.edu.cn

Abstract

The Indian Ocean Dipole (IOD) and the El Niño-Southern Oscillation (ENSO) are two major modes of interannual climate variability that interact across the Indo-Pacific region. Although the autumn IOD is known to influence ENSO with a lag of about one year, the decadal stability of this relationship remains poorly understood. Here we investigate the decadal variability of the lagged IOD–ENSO relationship using observations and 30 Coupled Model Intercomparison Project Phase 6 (CMIP6) models. Observational analyses reveal pronounced non-stationarity in the lagged IOD-ENSO linkage, characterized by a stronger (weaker) relationship during the negative (positive) phase of the Atlantic Multidecadal Oscillation (AMO). CMIP6 models exhibit a wide spread in their ability to reproduce this behavior, with only a subset capturing the observed decadal modulation. The inter-model differences are consistent with variations in the simulated amplitude of AMO variability. Models with more realistic AMO variability tend to better reproduce the observed decadal variability of the lagged IOD-ENSO linkage. These results suggest that AMO variability may be one contributing factor to the modulation of the lagged IOD–ENSO relationship, with potential implications for ENSO prediction.

Keywords: Indian Ocean Dipole (IOD); El Niño-Southern Oscillation (ENSO); decadal variability; inter-basin interaction

1. Introduction

The Indian Ocean Dipole (IOD) and the El Niño-Southern Oscillation (ENSO) are two dominant modes of interannual climate variability that exert widespread impacts on global weather and climate [1–5]. These two modes are not independent, but interact through air–sea coupling processes across the Indo-Pacific region, leading to significant variability in their respective evolution and teleconnections [6–10]. Among these interactions, increasing attention has been paid to the delayed influence of the boreal autumn IOD on ENSO in the following year, as it provides an important source of ENSO predictability beyond the spring predictability barrier [11–15].

The mechanisms underlying the lagged IOD–ENSO relationship have been extensively investigated. Previous studies have proposed that atmospheric bridge represents a primary pathway, whereby IOD-induced Walker circulation anomalies modify wind stress and ocean–atmosphere conditions over the tropical Pacific, thereby favoring ENSO development in the following year [12,14,16–18]. In addition, oceanic pathways associated with the Indonesian Throughflow have been proposed as another important mechanism through

Check for updates

Academic Editor: Dae Il Jeong

Received: 23 June 2026
Revised: 3 August 2026
Accepted: 10 August 2026
Published: 24 August 2026

Copyright: © 2026 by the authors. Licensee MDPI, Basel, Switzerland. This article is an open access article distributed under the terms and conditions of the Creative Commons Attribution (CC BY) license.

which Indian Ocean anomalies can be transmitted into the Pacific and affect ENSO's subsequent evolution [19–23]. Recently, inter-basin interaction mechanisms involving the Atlantic Ocean have also been proposed. In particular, the so-called "IOD-Atlantic-ENSO" pathway suggests a two-stage process in which positive IOD events can trigger Atlantic Niño conditions, which in turn influence ENSO development through tropical Atlantic–Pacific teleconnections [13,24,25]. These mechanisms highlight the fact that the delayed IOD–ENSO relationship emerges from multiple interacting atmospheric and oceanic processes across tropical basins.

Growing evidence suggests that the lagged IOD–ENSO relationship exhibits pronounced decadal variability [26–28]. Observational analyses show that the relationship between the boreal autumn IOD and the following winter ENSO was relatively weak during 1930–1960. However, from the mid-1970s onward, the lagged correlation strengthened and remained relatively strong until the 1990s [27]. This decadal fluctuation in coupling strength does not exhibit a simple linear trend, but instead exhibits marked transitions between different epochs, suggesting potential modulation by decadal climate variability [29]. This decadal variability has important implications for ENSO predictability. When the lagged IOD–ENSO relationship is strong, Indian Ocean conditions provide useful predictive signals for ENSO evolution at approximately one-year lead time. In contrast, when the relationship weakens, the predictive utility of IOD-related signals declines, potentially reducing forecast skill [30]. Understanding the causes of this non-stationarity is therefore important for improving the reliability of ENSO prediction.

The observed decadal variability of the lagged IOD–ENSO relationship raises an important question regarding its relationship with decadal climate modes. While several studies have suggested that decadal climate variability may play a role in modulating the lagged IOD–ENSO relationship, its relationship with major modes of climate variability remain unclear [27,31]. In particular, the Atlantic Multidecadal Oscillation (AMO) has been proposed as a possible factor associated with changes in tropical inter-basin interactions [32–34]. Climate models provide an essential tool for understanding and simulating variability in inter-basin interactions [35–37]. Therefore, assessing whether state-of-the-art models can reproduce the observed decadal modulation of the lagged IOD–ENSO relationship is a necessary step toward understanding the robustness of simulated Indo-Pacific teleconnections. In this study, we analyze 30 CMIP6 models to evaluate their ability to reproduce the observed decadal variability of the lagged IOD–ENSO relationship. We hypothesize that differences in the representation of AMO variability among models may contribute to their divergent capabilities in simulating this decadal modulation.

2. Data and Methods

2.1. Data

Monthly sea surface temperature (SST) data are obtained from the NOAA Extended Reconstructed Sea Surface Temperature version 4 (ERSSTv4; 1900–2014) [38]. Monthly outputs of historical simulations of 30 models each from CMIP6 are utilized (see Table 1). We selected the time period from January 1900 to December 2014 in this study, the same as in the observations. All data were interpolated onto a common $1^\circ \times 1^\circ$ grid for multi-model ensemble (MME) mean analysis. Only one ensemble member is considered. To exclude the influence of global warming, long-term linear trends in variables are removed using the least squares method. A 21-year running mean is applied to extract the dominant signals on decadal timescales.

Table 1. Information on the 30 CMIP6 model datasets used in this study.

Model Name	Country	Resolution	Model Name	Country	Resolution
AWI-CM-1-1-MR	Germany	384 × 192	EC-Earth3	Europe	512 × 256
CAMS-CSM1-0	China	320 × 160	FIO-ESM-2-0	China	288 × 192
CanESM5-1	Canada	128 × 64	GISS-E2-1-G-CC	USA	144 × 90
CAS-ESM2-0	China	256 × 128	GISS-E2-1-G	USA	144 × 90
CESM2-FV2	USA	144 × 96	HadGEM3-GC31-LL	UK	432 × 324
CESM2-WACCM-FV2	USA	144 × 96	HadGEM3-GC31-MM	UK	432 × 324
CESM2-WACCM	USA	288 × 192	IPSL-CM6A-LR	France	144 × 143
CESM2	USA	288 × 192	MIROC-ES2L	Japan	256 × 128
CMCC-ESM2	Italy	288 × 192	MIROC6	Japan	256 × 128
CNRM-CM6-1	France	256 × 128	MPI-ESM-1-2-HAM	Germany	384 × 192
CNRM-ESM2-1	France	256 × 128	MPI-ESM1-2-HR	Germany	384 × 192
E3SM-1-0	USA	360 × 180	MPI-ESM1-2-LR	Germany	384 × 192
E3SM-1-1-ECA	USA	360 × 180	NESM3	China	192 × 96
E3SM-1-1	USA	360 × 180	SAM0-UNICON	Republic of Korea	288 × 192
EC-Earth3-Veg	Europe	512 × 256	UKESM1-0-LL	UK	192 × 145

2.2. Index Definitions

The Niño 3.4 index quantifies ENSO variability, defined as area-averaged SST anomalies over 5° S–5° N, 170° W–120° W [39]. The Dipole Mode Index (DMI) quantifies IOD variability, defined as the difference in area-averaged SST anomalies between the western Indian Ocean (10° S–10° N, 50° E–70° E) and eastern Indian Ocean (10° S–0°, 90° E–110° E) boxes [1]. The Atlantic Niño index is defined as area-averaged SST anomalies over 15° S–5° N, 30° W–10° E following Fan and Meng [13]. The Atlantic Multidecadal Oscillation (AMO) index is computed as the annual mean SST anomalies averaged over the North Atlantic basin, spanning latitudes from the equator to 60° N. The autumn refers to September, October and November (SON). The numbers 0 and +1 in parentheses indicate that the month belongs to the same year and the ensuing year of the DMI, respectively. The Walker circulation is represented by zonal and vertical wind anomalies averaged over 10° S–5° N.

2.3. Statistical Significance Test

The statistical significance of decadal-scale linear regression and correlation is assessed using a two-tailed Student's *t*-test. To account for the reduction in degrees of freedom due to autocorrelation, the effective sample size is estimated following Bretherton et al. [40]. In this framework, the effective number of degrees of freedom N^* is defined as:

$$N^* \approx N \frac{1 - R_x R_y}{1 + R_x R_y}, \quad (1)$$

where N is the original sample size, N^* is the effective sample size, and R_x and R_y denote the lag-1 autocorrelation coefficients of variables x and y, respectively.

3. Results

3.1. Observed Decadal Variability of the Lagged IOD–ENSO Relationship

The IOD typically peaks in boreal autumn and decays during winter, providing a potential precursor for ENSO evolution in the subsequent year. Following Izumo et al. (2010) [12], the lagged relationship between the IOD and ENSO is characterized using the SON (0) DMI and the OND (+1) Niño3.4 index, corresponding to an approximately 14-month lead time. To examine the stability of this linkage on decadal timescales, a 21-year sliding correlation is applied to the standardized SON (0) DMI and OND (+1) Niño3.4 index. As shown in Figure 1a, the lagged IOD–ENSO relationship exhibits pronounced

decadal variability, with strong negative correlations occurring before 1920 and during 1970–2000, and weak negative or even positive correlations prevailing during 1920–1960 and after 2000 (Figure 1a, red solid line).

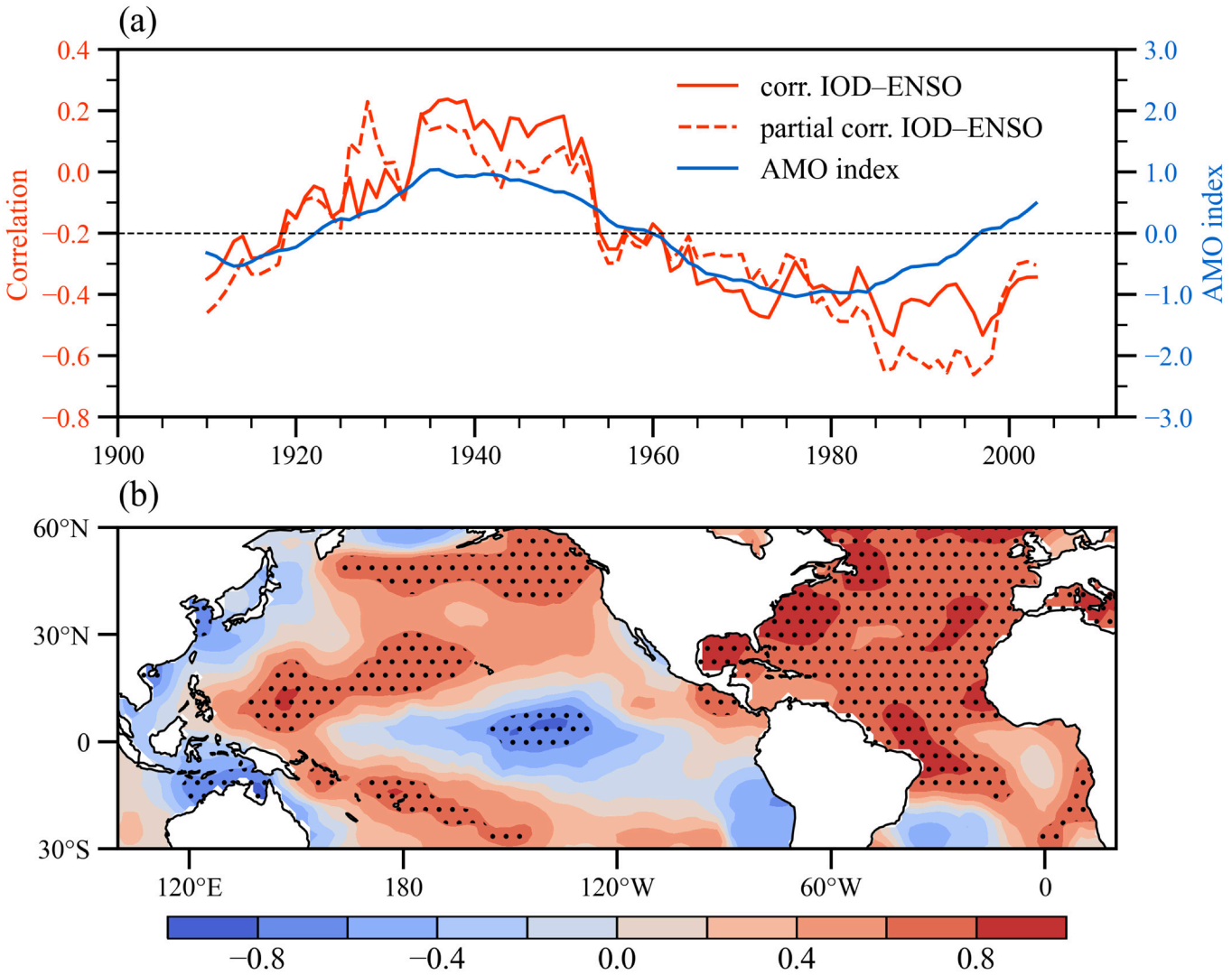


Figure 1. Connection between the decadal variation in the IOD–subsequent-year-ENSO relationship and the AMO. (**a**) Decadal variation in the IOD–subsequent-year-ENSO relationship (red solid line), decadal variation in IOD–subsequent-year-ENSO relationship after removing the D (0) JF (+1) ENSO effect (red dotted line) and the 21-year running mean normalized AMO index (blue line). The time-varying relationship between the IOD and following-year ENSO is measured by the 21-year sliding interannual correlation between the DMI in SON (0) and the Niño 3.4 index in OND (+1). (**b**) Correlation map of the 21-year sliding correlation between SON (0) DMI and OND (+1) Niño 3.4 with decadal SST anomalies (1900–2014). The decadal SST anomalies are derived from a 21-year sliding mean. Dotted shading indicates correlations that are statistically significant at the 95% confidence level.

Previous studies have suggested that decadal climate variability may play a role in modulating Indo-Pacific interactions, with the Atlantic Multidecadal Oscillation (AMO) proposed as a potential contributor. We therefore examine whether observed decadal modulation of the IOD–ENSO relationship is associated with the AMO. Figure 1b shows the correlation between the decadal variability of the lagged IOD–ENSO relationship and global SST anomalies, revealing significant positive correlations across the North Atlantic basin, a pattern broadly consistent with the AMO. This result suggests that the AMO

provides an important large-scale background for the decadal modulation of the lagged IOD–ENSO relationship. Although stronger (weaker) coupling generally occurs during negative (positive) AMO phases (Figure 1a), deviations from this tendency indicate that other modes of decadal climate variability may also contribute during specific periods. Notably, this relationship remains robust after linearly removing the influence of concurrent ENSO variability in D (0) JF (+1) (Figure 1a, red dotted line), indicating that the observed decadal modulation is not solely attributable to ENSO autocorrelation.

3.2. Evaluation of the Lagged IOD–ENSO Relationship in CMIP6 Models

Motivated by the observed decadal modulation of the lagged IOD–ENSO relationship, this section evaluates the performance of CMIP6 models in three steps. First, we examine whether the models reproduce the basic characteristics of the IOD and ENSO, including their seasonal phase-locking and quasi-biennial variability, and select a subset of models that reasonably capture these fundamental features. Second, using this selected subset, we assess the ability of the models to reproduce the observed relationship between the autumn IOD and the following year's ENSO. Finally, we investigate whether the models can represent the decadal variability of this lagged relationship and its association with the AMO.

3.2.1. Simulation of the Basic Characteristics of IOD and ENSO in CMIP6 Models

Because the lagged IOD–ENSO relationship is strongly season-dependent, CMIP6 models must first reproduce the observed seasonal phase-locking characteristics of both the IOD and ENSO. We first examine the seasonal phase locking of IOD and ENSO in 30 CMIP6 models (Figure 2a,b). In observations (bold black lines), IOD peaks in SON and ENSO in DJF. For IOD, 26 models capture the SON peak, while four models show a peak outside SON (dashed gray lines in Figure 2a), consistent with earlier findings [41]. For ENSO, four models simulate a peak in spring or summer, opposite to the observed winter peak (dashed gray lines in Figure 2b). This common bias likely arises from difficulties in simulating key ENSO dynamics [42]. These eight models are therefore excluded, leaving 22 models for subsequent analyses. A summary of the seasonal phase-locking characteristics and model selection for all 30 CMIP6 models is provided in Table S1. All following results are based on this selected ensemble.

After selecting models based on seasonal phase-locking, we further examine their ability to reproduce the quasi-biennial tendency of ENSO and IOD, which is necessary to distinguish IOD-induced variability from ENSO's intrinsic oscillation. Most CMIP6 models capture ENSO's quasi-biennial tendency, although the amplitude at a one-year lag is systematically overestimated in many models (Figure 2d). In observations, the quasi-biennial tendency of the IOD is weaker and less regular. The CMIP6 multi-model ensemble broadly reproduces this feature, but with a weaker secondary peak at one-year lag (Figure 2c). These results highlight the need to account for ENSO self-oscillation when assessing the lagged IOD–ENSO relationship.

3.2.2. Simulation of the Lagged IOD–ENSO Relationship in CMIP6 Models

Using the 22 models that reasonably capture the basic characteristics of the IOD and ENSO, we further evaluate their ability to reproduce the observed lagged relationship between the autumn IOD and the following year's ENSO.

Figure 3a shows the lead-lag partial correlations between SON (0) DMI and the Niño3.4 index in observations (black line) and CMIP6 models (colored lines), with the concurrent ENSO signal removed. In observations, the SON (0) DMI is significantly negatively correlated with the OND (+1) Niño3.4 index, with a correlation coefficient of -0.27, indicating an approximately 14-month lagged relationship between the autumn IOD and the fol-

lowing year's ENSO. Most CMIP6 models reproduce this negative lagged relationship, although the simulated correlation strength varies substantially across models, ranging from −0.11 to −0.62. Many models simulate stronger negative correlations than observed, while two models, HadGEM3-GC31-LL and HadGEM3-GC31-MM, produce negative but statistically insignificant correlations. In addition to differences in correlation strength, some models exhibit biases in the timing of the maximum negative correlation, with the strongest relationship occurring one or two seasons earlier or later than in observations. These discrepancies highlight substantial inter-model spread in simulating the timing and strength of the lagged IOD–ENSO connection.

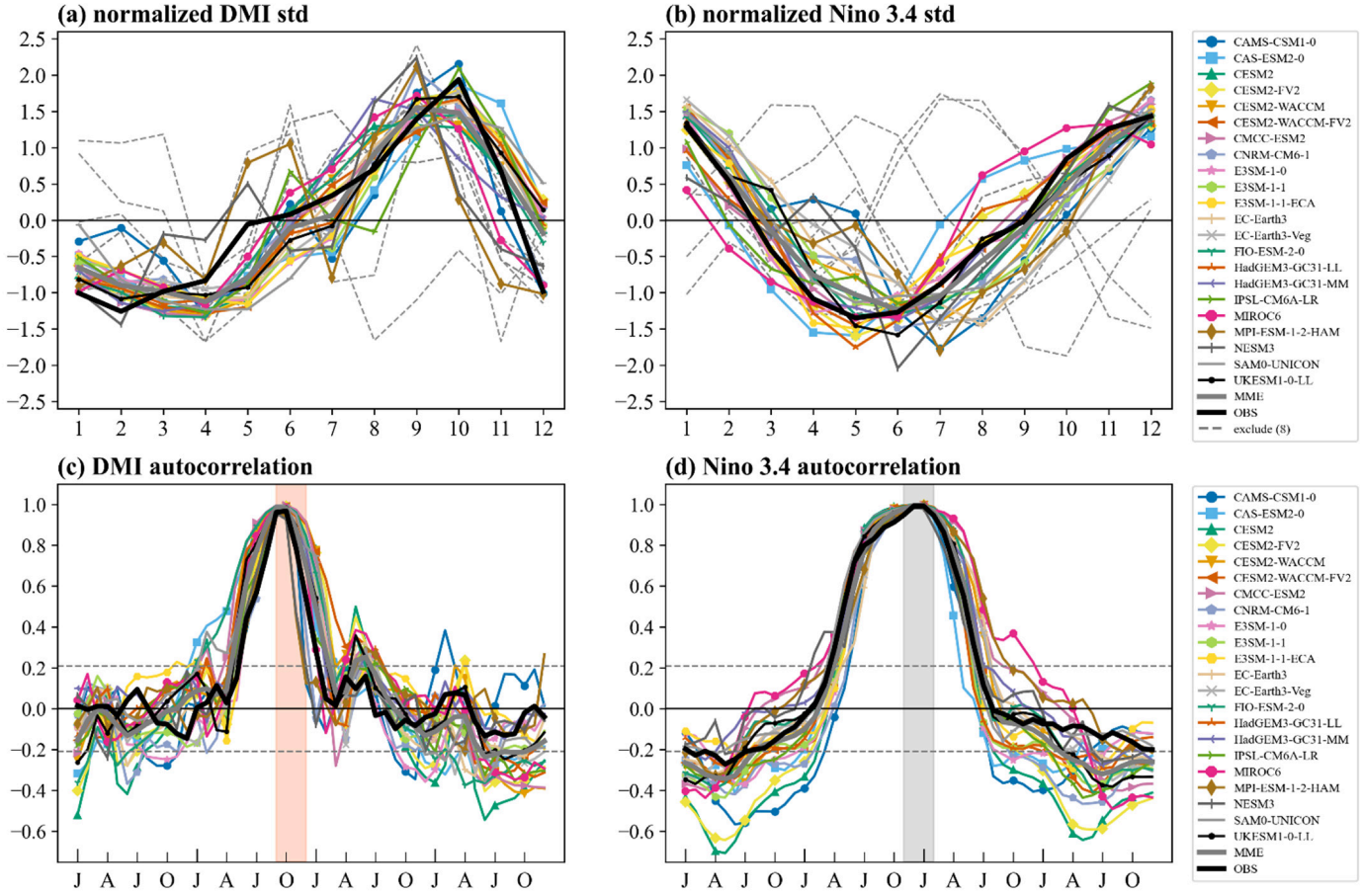


Figure 2. Seasonal cycles and autocorrelations of IOD and ENSO in CMIP6 models. (**a**,**b**) Normalized standard deviations of (**a**) DMI and (**b**) Niño 3.4 index. Colored thin lines represent individual models, bold gray line shows multi-model ensemble (MME) mean, and bold black line represents observations (OBS). Dashed gray lines indicate models that misrepresent the seasonal phase-locking of either IOD or ENSO; these models are excluded from subsequent analysis. (**c**,**d**) Autocorrelations of (**c**) SON DMI and (**d**) NDJ Niño 3.4. Pink and gray bars mark represent zero lag for IOD and ENSO, respectively. Dashed line indicates 95% confidence level. MME (bold gray) and observations (bold black) are also shown. The letters J, A, J, and O denote January, April, July, and October, respectively.

To facilitate a quantitative comparison among models, Figure 3b summarizes the partial correlation coefficients at the observed 14-month lag for selected 22 CMIP6 models, together with the observations and the multi-model ensemble (MME). The observed correlation coefficient is −0.27 (gray dashed line), while the MME reproduces a comparable value of −0.36, indicating that the ensemble mean reasonably captures the observed lagged IOD–ENSO relationship. Nevertheless, considerable inter-model spread remains, with individual models exhibiting substantially stronger or weaker lagged correlations than observed. Using the observed correlation coefficient (−0.27) as an objective threshold,

models with correlation values lower than −0.27 are considered to reproduce the observed lagged relationship and are therefore retained for subsequent analyses. Based on this criterion, 16 models are selected, while the remaining models are excluded.

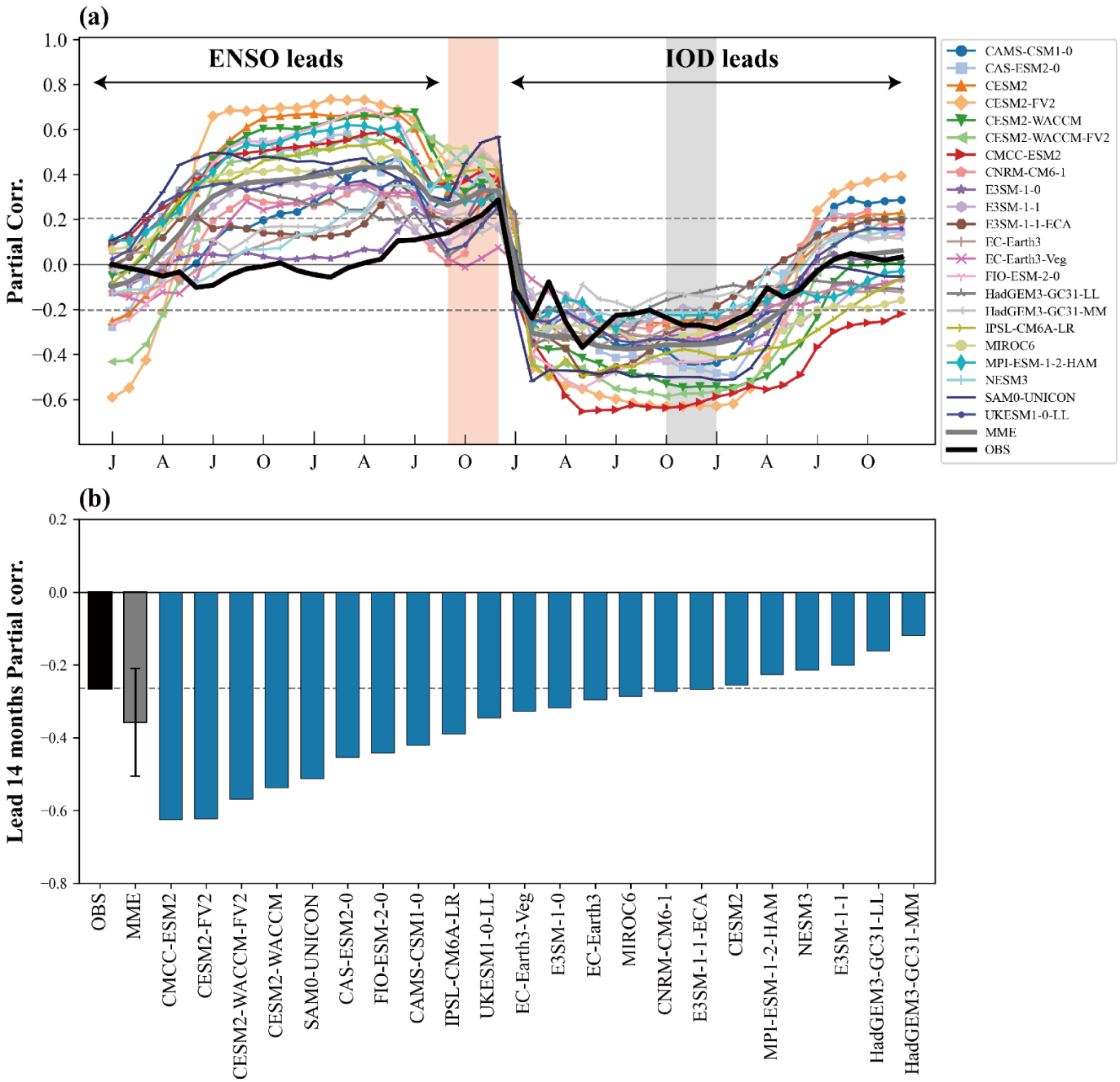


Figure 3. Lead-lag partial correlations between the SON (0) DMI and Niño 3.4 index in CMIP6 models. (**a**) Partial correlations with the D (0) JF (+1) ENSO signal removed; colored thin lines denote individual models, the bold gray line denotes the multi-model ensemble (MME) mean, and the bold black line denotes observations (OBS). The pink and gray shadings mark the IOD peak season and the ENSO peak season (~14 months after the IOD peak), respectively. Black dashed lines denote the 95% confidence level. (**b**) Partial correlations at the 14-month lag, sorted in ascending order for the 22 selected models (blue bars). The black and gray bars represent OBS and MME, respectively. Error bar on MME indicates one standard deviation across the selected models. The gray dashed line marks the observed correlation value.

3.2.3. Representation of Decadal Variability in the Lagged IOD–ENSO Relationship

Using the subset of CMIP6 models that reasonably reproduce the IOD-following year's ENSO relationship, we further examine whether they capture the observed decadal variability of this relationship and its association with the AMO. In observations, the lagged IOD–ENSO relationship shows a clear phase dependence. The correlation is weak and statistically insignificant during positive AMO phases, but becomes stronger and statistically significant during negative AMO phases. Specifically, the partial correlation between SON (0) DMI and OND (+1) Niño3.4 is −0.169 during positive AMO phases and −0.358 during negative AMO phases (Figure 4a), indicating a strengthened lagged connection under negative AMO conditions.

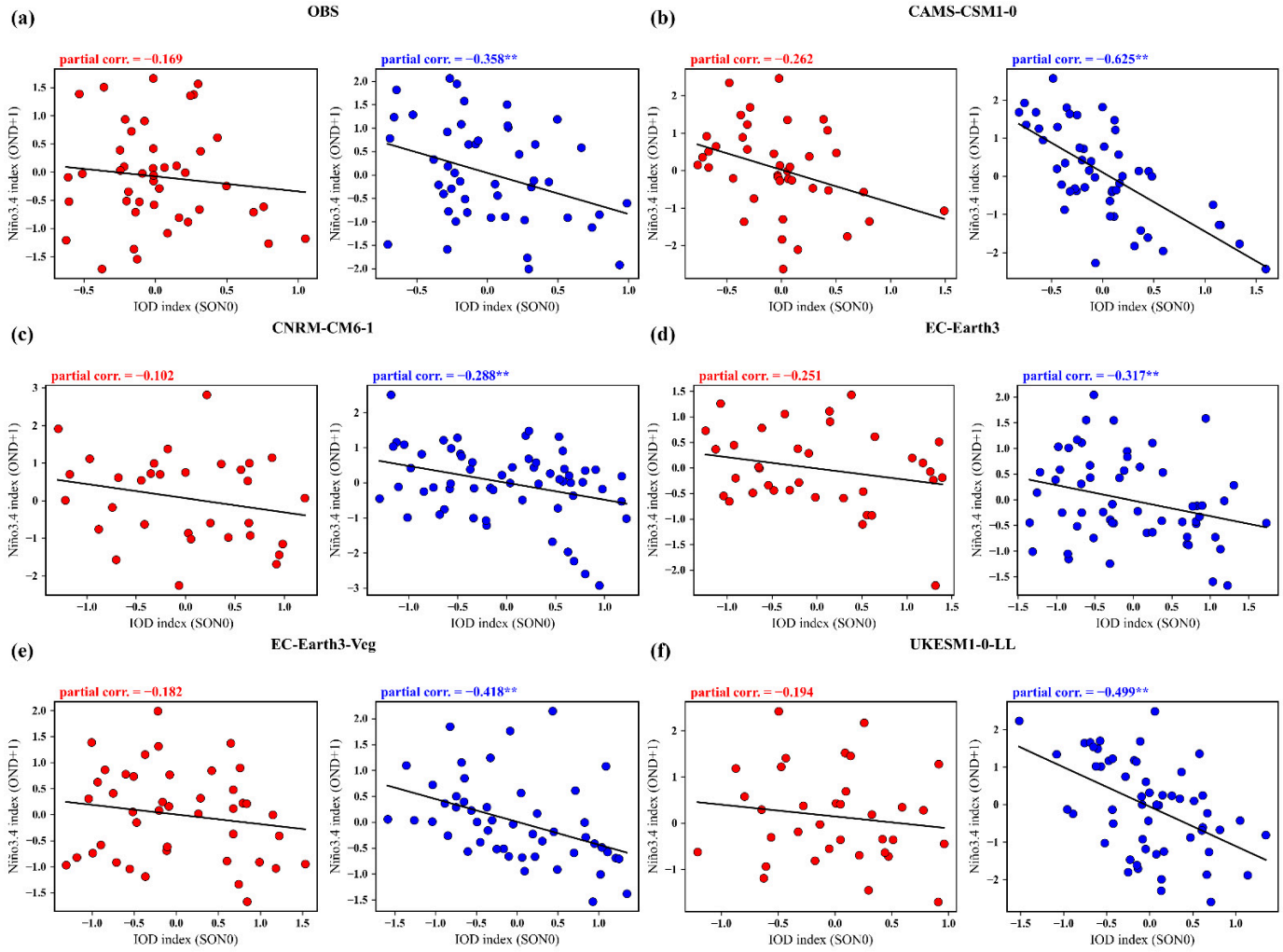


Figure 4. Partial correlation scatter plots of SON (0) DMI versus OND (+1) Niño 3.4 index under different AMO phases. (**a**) Observations and (**b**–**f**) CMIP6 high-capability group (HCG) models: CAMS-CSM1-0, CNRM-CM6-1, EC-Earth3, EC-Earth3-Veg, and UKESM1-0-LL. Within each panel, the left (right) subplot corresponds to the positive (negative) AMO phase. Red (blue) dots denote the respective phase years, and black lines show the least-squares linear fit. Values in the upper-right corner are partial correlation coefficients; * and ** indicate significance at the 90% and 95% confidence levels, respectively.

Based on their ability to reproduce this observed phase-dependent contrast, the CMIP6 models are classified into two groups (Table S2). The high-capability group (HCG; five models) consists of models that successfully capture the observed AMO-related modulation, characterized by weaker or statistically insignificant IOD–ENSO correlations during

positive AMO phases and stronger negative correlations during negative AMO phases (Figure 4). This behavior is broadly consistent with observations and indicates that these models can represent the observed decadal variability of the lagged IOD–ENSO relationship. In contrast, the low-capability group (LCG; six models) exhibits an opposite phase dependence. In these models, the lagged IOD–ENSO relationship is generally stronger during positive AMO phases than during negative AMO phases, contrary to the observed behavior (Figure 5). The corresponding partial correlation coefficients for each model under positive and negative AMO phases are summarized in Table S2, which provides a quantitative basis for the classification of model capability. Models that do not show a consistent or robust phase-dependent response are not included in either group. This contrast between the HCG and LCG indicates substantial inter-model differences in representing the AMO-associated decadal modulation of the IOD–ENSO teleconnection.

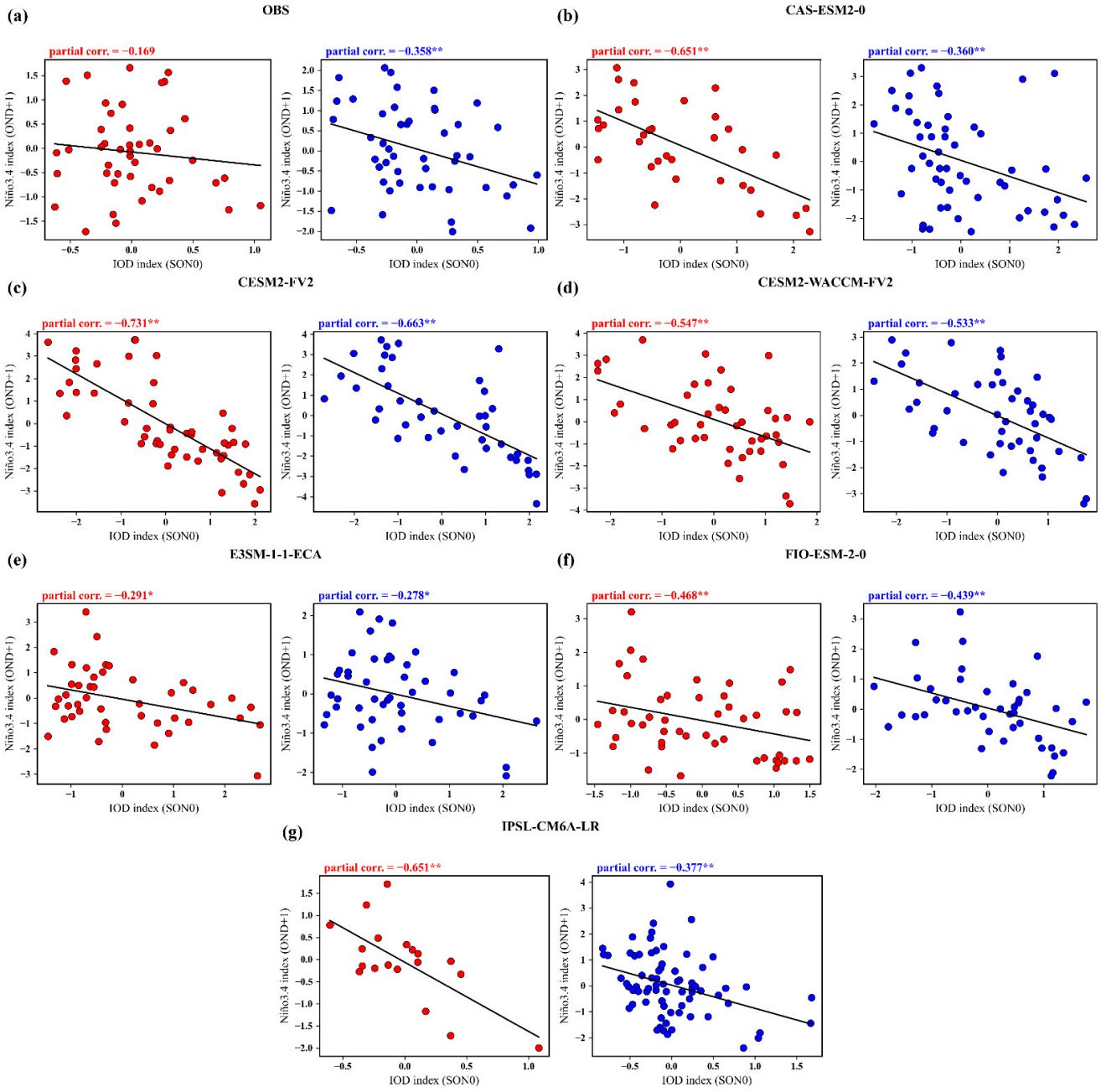


Figure 5. Partial correlation scatter plots of SON (0) DMI versus OND (+1) Niño 3.4 index under different AMO phases. (**a**) Observation and (**b**–**g**) CMIP6 low-capability group (LCG) models: CAS-

ESM2-0, CESM2-FV2, CESM2-WACCM-FV2, E3SM-1-1-ECA, FIO-ESM-2-0, and IPSL-CM6A-LR. Within each panel, the left (right) subplot corresponds to the positive (negative) AMO phase. Red (blue) dots denote the respective phase years, and black lines show the least-squares linear fit. Values in the upper-right corner are partial correlation coefficients; * and ** indicate significance at the 90% and 95% confidence levels, respectively.

3.3. AMO-Related Modulation of Model Differences in the Decadal Lagged IOD–ENSO Relationship

Based on the classification in Section 3.2, CMIP6 models are grouped into a high-capability group (HCG) and a low-capability group (LCG) according to their ability to reproduce the AMO-related modulation of the lagged IOD–ENSO relationship. To diagnose the physical processes associated with this inter-model discrepancy, we compare the multi-model ensemble (MME) mean responses of air–sea coupling over the Indo-Atlantic-Pacific sector, focusing on the seasonal evolution of SST, 925 hPa winds, Walker circulation, and sea surface height anomalies (Figures 6–8).

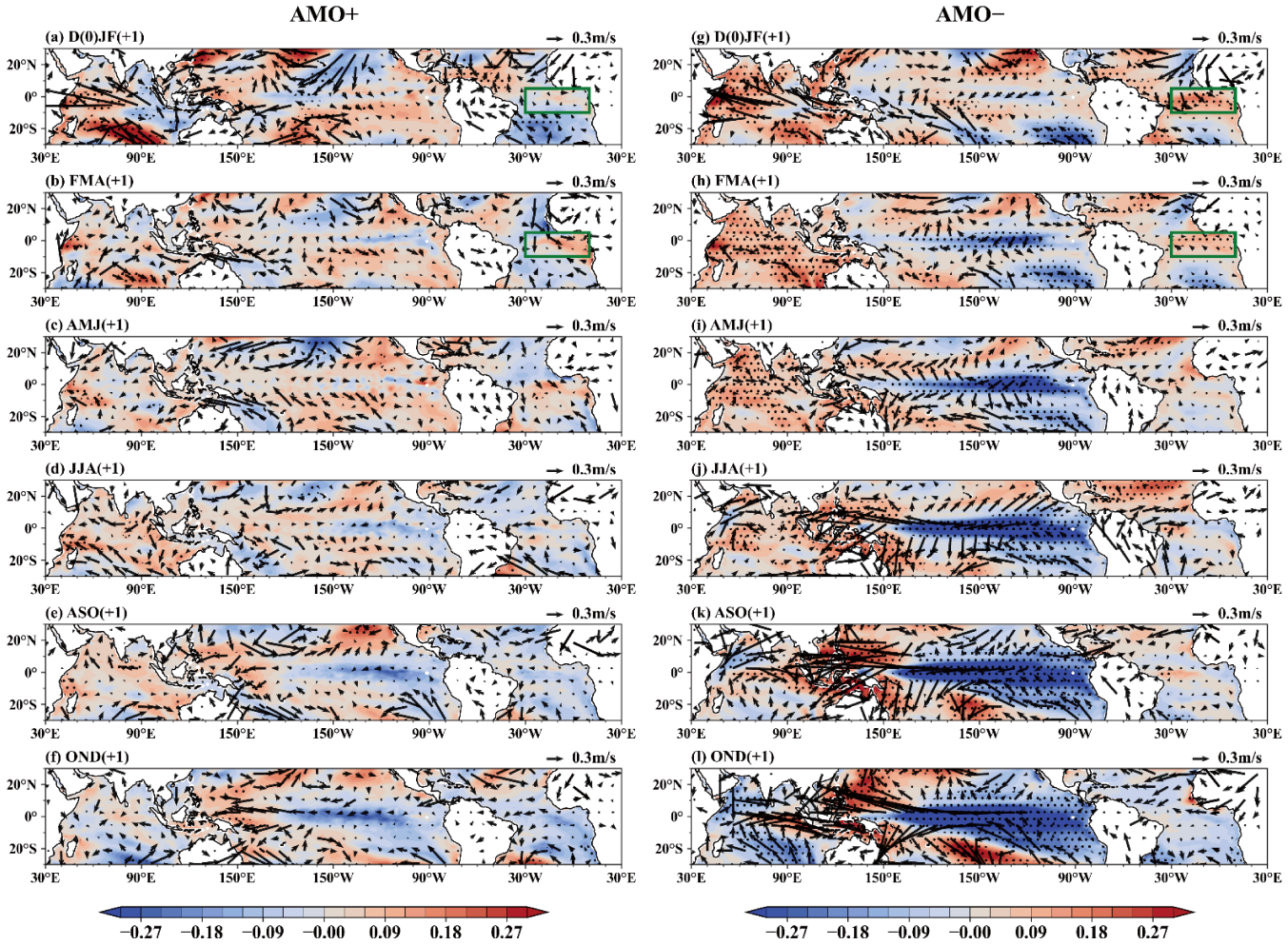


Figure 6. Lagged partial regression of SST anomalies (shading, °C) and 925 hPa wind anomalies (vectors, m s^{-1}) onto the normalized SON (0) DMI in the HCG multi-model ensemble mean. (**a**–**f**) AMO positive phase; (**g**–**l**) AMO negative phase. The concurrent ENSO effect is removed by linearly regressing on the D (0) JF (+1) Niño 3.4 index. Dotted area indicates that the regressions are significant at 95% confidence level. Green boxes indicate the Atlantic Niño area.

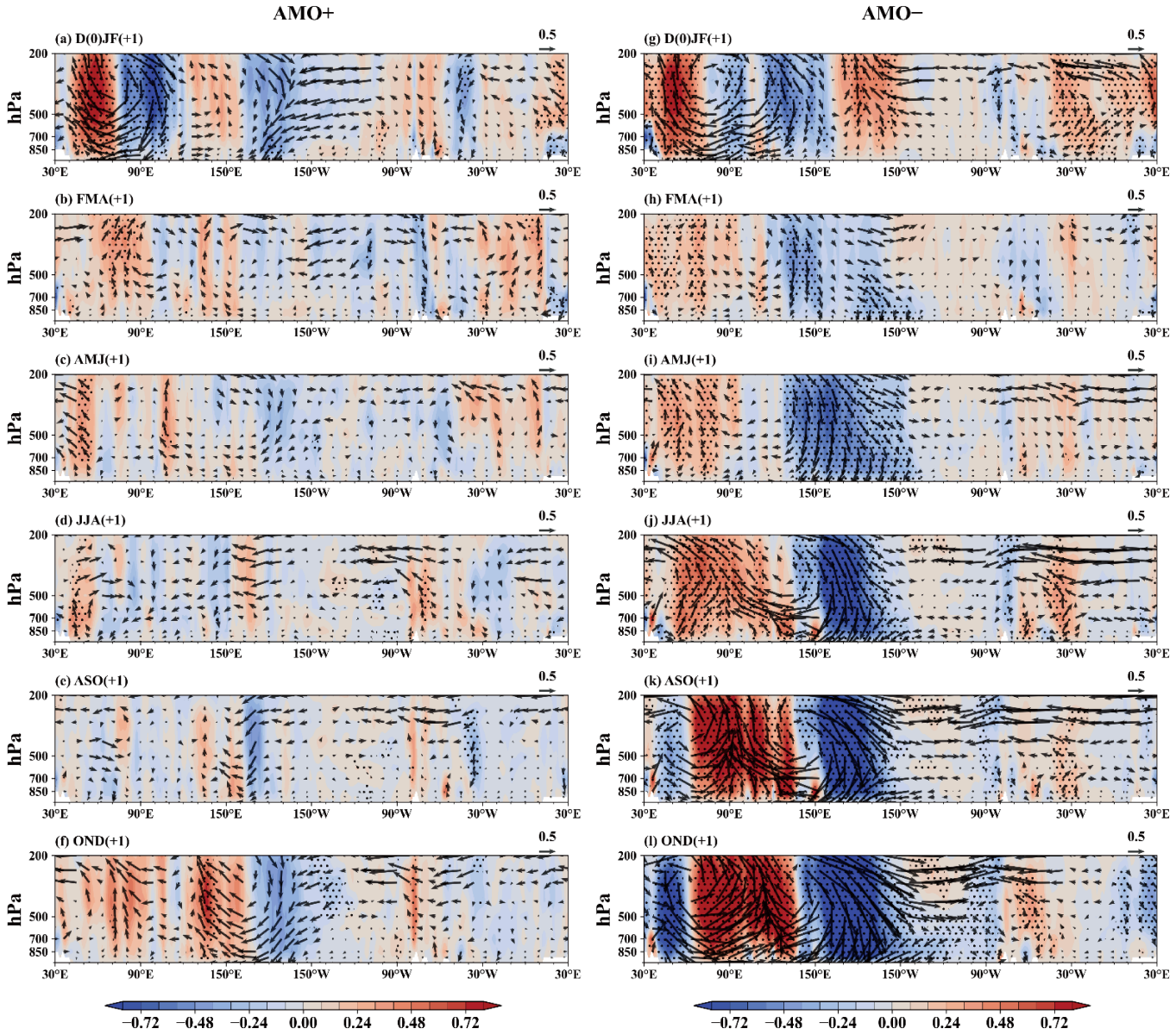


Figure 7. Lagged partial regression of the equatorial Walker circulation (10° S–5° N averaged) onto the normalized SON (0) DMI in the HCG multi-model ensemble mean. (**a**–**f**) AMO positive phase; (**g**–**l**) AMO negative phase. Shading denotes vertical velocity anomalies (Pa s^{-1}), and vectors represent the composite of zonal wind (u, m s^{-1}) and vertical velocity (ω, Pa s^{-1}), with ω multiplied by −100 for scaling. The concurrent ENSO signal is removed by linearly regressing on the D (0) JF (+1) Niño 3.4 index. Dotted area indicates that the regressions are significant at 95% confidence level.

In the HCG, the IOD-related inter-basin response exhibits a clear dependence on the AMO phase. During negative AMO phases, a coherent Indo-Atlantic-Pacific teleconnection pathway emerges. Positive IOD events are associated with westerly wind anomalies over the tropical Atlantic in boreal winter, followed by the development of an Atlantic Niño-like SST warming over the equatorial Atlantic (Figures 6g and 8g). This Atlantic Niño-like warming is accompanied by anomalous easterly winds over the central equatorial Pacific (Figure 7g–k), which favor the development of a La Niña-like SST pattern through coupled ocean–atmosphere feedbacks. The associated circulation pattern suggests a basin-scale reorganization of the Walker circulation extending across the Indo-Atlantic-Pacific sector. During positive AMO phases, these Atlantic and Pacific responses are substantially weaker and shorter-lived, indicating a suppressed inter-basin teleconnection.

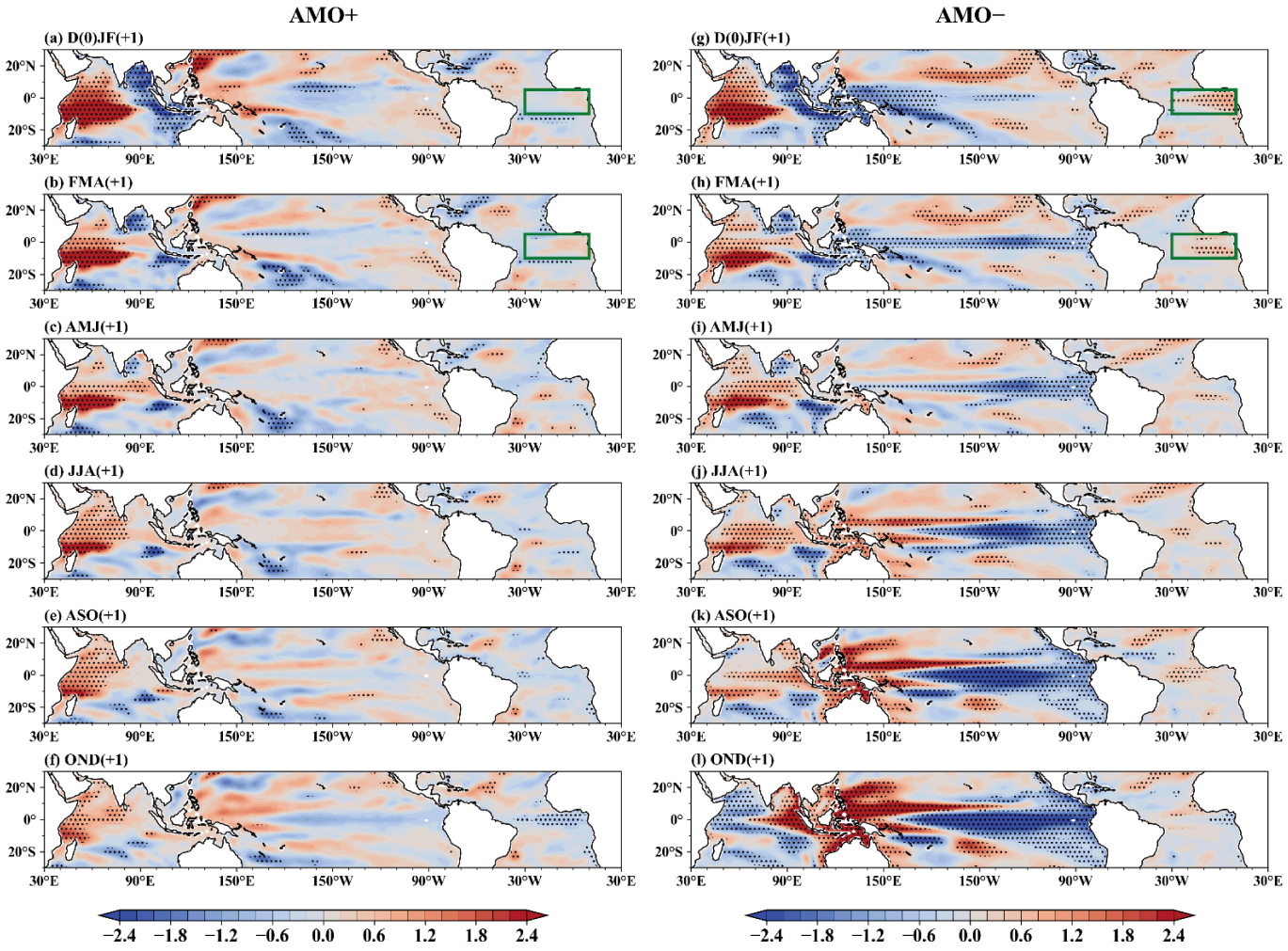


Figure 8. Lagged partial regression of sea surface height anomalies (shading, 10^{-2} m) onto the normalized SON (0) DMI in the HCG multi-model ensemble mean. (**a**–**f**) AMO positive phase; (**g**–**l**) AMO negative phase. The concurrent ENSO signal is removed by linearly regressing on the D (0) JF (+1) Niño 3.4 index. Dotted area indicates that the regressions are significant at 95% confidence level. The green box indicates the Atlantic Niño region.

In contrast, the LCG exhibits little sensitivity to the AMO phase. Similar Pacific SST and wind anomalies are present during both positive and negative AMO phases, and the associated Walker circulation anomalies show limited phase dependence (see in Supporting Information Figures S1–S3). In addition, the Atlantic Niño-like SST anomalies do not show a consistent weakening during positive AMO phases. This weak phase dependence suggests that the LCG does not effectively represent the AMO-related modulation of inter-basin coupling. The contrasting behaviors between the HCG and LCG indicate that the simulated tropical Atlantic response, particularly the Atlantic Niño-like SST warming, is closely linked to model fidelity in representing the AMO-associated modulation of the lagged IOD-ENSO teleconnection.

Figure 9 further indicates that these differences are closely associated with the simulated amplitude of the AMO. Observations exhibit a pronounced horseshoe-shaped SST anomaly pattern over the North Atlantic, with amplitudes of approximately 0.6–0.8 °C per standard deviation. The HCG reproduces both the spatial structure and magnitude of this variability reasonably well, whereas the LCG simulates substantially weaker AMO-related SST anomalies. The weaker AMO variability in the LCG is accompanied by a reduced sensitivity of the tropical Atlantic to decadal background-state changes, which may limit

the effectiveness of Atlantic-mediated inter-basin interactions. Consequently, the decadal modulation of the IOD–ENSO relationship is less evident in these models. While these results do not establish a direct causal link, they suggest that realistic simulation of AMO variability may be an important contributor to reproducing observed decadal fluctuations in Indo-Pacific teleconnections.

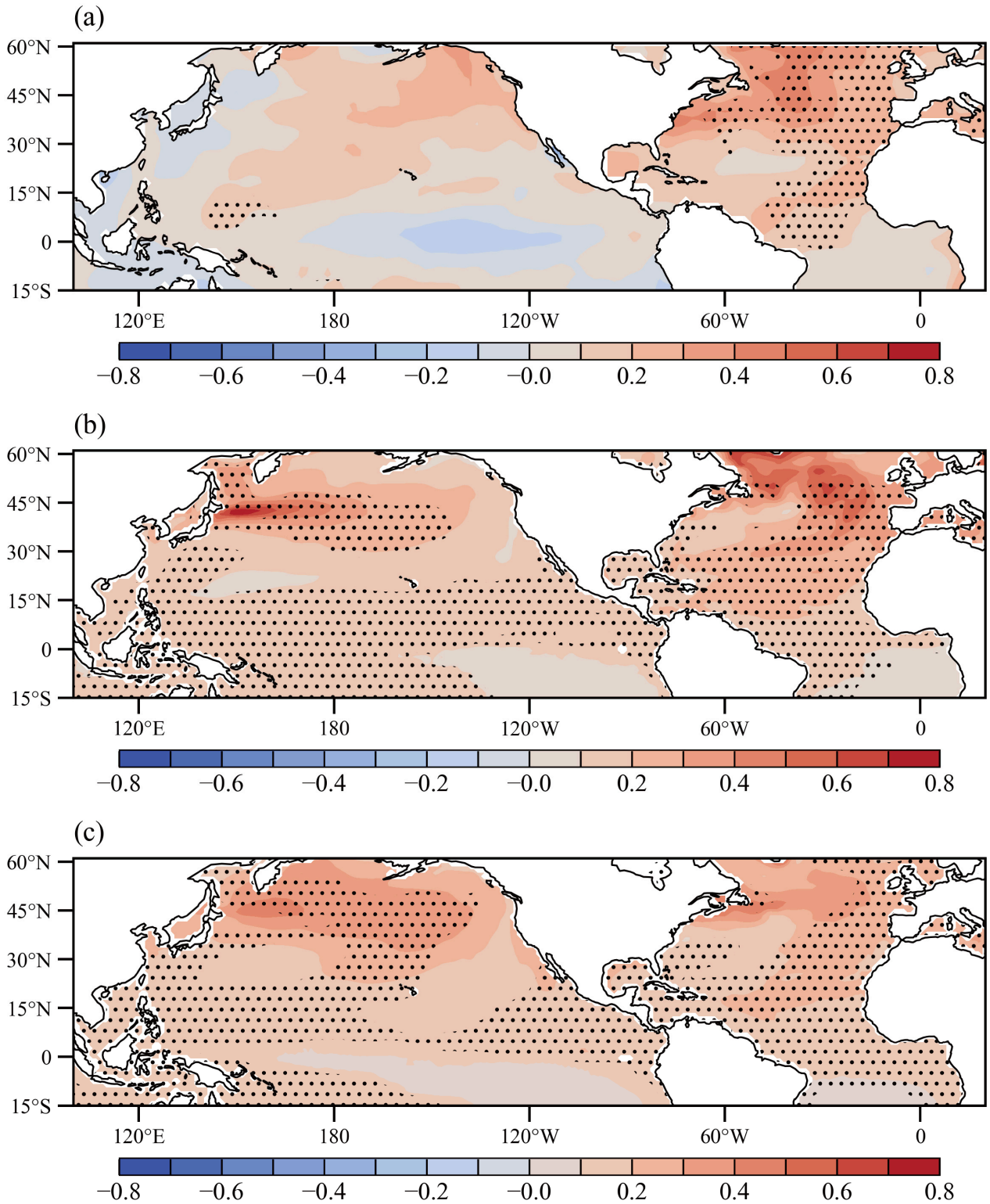


Figure 9. Regressions of SST anomalies onto the normalized AMO index. (**a**) Observations; (**b**) high-capability group (HCG) multi-model ensemble mean; (**c**) low-capability group (LCG) multi-model ensemble mean. The dotted areas indicate the 95% confidence level.

4. Discussion and Conclusions

Using observations and CMIP6 historical simulations, this study shows that the lagged relationship between the autumn IOD and the following-year ENSO is not stationary but undergoes pronounced interdecadal fluctuations associated with the phase of the AMO. Notably, this modulation is reproduced primarily by the high-capability group (HCG), whereas the low-capability group (LCG) largely fails to capture the observed decadal modulation, highlighting substantial inter-model diversity in representing inter-basin teleconnections on decadal timescales. This diversity is closely associated with differences in how models simulate the Atlantic's role as a mediating pathway between the Indian and Pacific Oceans, rather than with deficiencies in the basic seasonal or interannual characteristics of the IOD and ENSO themselves. These results indicate that realistic AMO variability is essential for reproducing the decadal modulation of Atlantic-mediated Indo-Pacific teleconnections.

A plausible explanation for the close relationship between AMO simulation skill and the representation of the decadal IOD–ENSO linkage is that the realism of simulated AMO variability reflects how well a model captures the coupled ocean–atmosphere processes governing North Atlantic low-frequency variability. Among these processes, the Atlantic Meridional Overturning Circulation (AMOC) is widely regarded as the dominant driver of multidecadal SST variability in the Atlantic and therefore plays a central role in determining the realism of simulated AMO variability [41–44]. Biases in the strength or variability of the AMOC can alter ocean heat transport and suppress the amplitude or persistence of AMO variability, leading to unrealistic multidecadal SST evolution in the North Atlantic [43,44]. Models that fail to reproduce realistic AMOC variability are therefore less likely to capture the Atlantic SST background state required for maintaining the Atlantic-mediated teleconnection linking the IOD and ENSO. In addition to AMOC, previous studies have suggested that biases in surface heat fluxes and NAO-related atmospheric variability may also affect the simulation of AMO by modulating North Atlantic SST persistence, mixed-layer processes, and air–sea coupling [45–48]. Although these processes are not explicitly diagnosed here, previous studies suggest that improving their representation may enhance simulations of Atlantic-mediated decadal Indo-Pacific teleconnections.

Our findings also extend previous understanding of the Atlantic pathway linking the IOD and ENSO. Previous studies have shown that the Atlantic Ocean acts as an important bridge through which the IOD influences the subsequent evolution of ENSO [13]. These studies mainly focused on the teleconnection mechanism operating on interannual timescales. However, whether this Atlantic-mediated pathway remains stationary across different decadal background states has received much less attention. By combining observations with CMIP6 historical simulations, the present study demonstrates that the strength of the Atlantic-mediated pathway varies with the AMO phase. Consequently, the lagged IOD–ENSO relationship exhibits pronounced interdecadal modulation rather than remaining stationary across different background climate states.

The implications of these findings extend beyond understanding the physical mechanism linking the IOD and ENSO and are also relevant to climate prediction and model evaluation. Because the strength of the lagged IOD–ENSO relationship varies with the AMO phase, the predictive value of the autumn IOD cannot be regarded as stationary. During negative AMO phases, the stronger Atlantic-mediated teleconnection suggests that the autumn IOD may provide a more reliable precursor for subsequent ENSO development. In contrast, this precursor relationship becomes weaker during positive AMO phases, implying reduced predictive skill. From a modeling perspective, our results suggest that evaluating climate models solely on their ability to reproduce the individual characteristics of ENSO or the IOD may be insufficient for assessing their capability to

simulate inter-basin climate interactions. Accordingly, the HCG models identified here provide a useful reference for studies of Atlantic-mediated Indo-Pacific teleconnections and seasonal-to-interannual climate prediction.

Despite the physical interpretation and broader implications discussed above, several uncertainties remain in interpreting the simulated decadal modulation of the lagged IOD–ENSO relationship. First, CMIP6 models are known to exhibit a systematic bias toward overly strong negative IOD variability, while recent studies suggest that negative IOD events transmit their influence to the Pacific through the Atlantic pathway less efficiently than positive IOD events [49,50]. Such event asymmetry may affect the simulated strength of the lagged IOD–ENSO relationship and therefore contribute to uncertainty in the representation of its modulation by the AMO. In addition, although the present study suggests that AMOC and other Atlantic processes contribute to inter-model differences in AMO simulation skill, these mechanisms were not directly diagnosed. Future work should therefore explicitly quantify the respective contributions of AMOC variability, surface heat fluxes, and NAO-related atmospheric variability to the simulated AMO and the associated Atlantic-mediated teleconnection. Targeted numerical experiments, such as pacemaker simulations or partially coupled model experiments, would further help isolate the causal roles of Atlantic variability and air–sea coupling in modulating the decadal IOD–ENSO relationship.

Overall, this study demonstrates that the decadal modulation of the lagged IOD–ENSO relationship is closely linked to the phase of the AMO and that CMIP6 models capable of realistically simulating AMO variability more successfully reproduce this modulation. These findings extend previous understanding of the Atlantic-mediated IOD–ENSO pathway by highlighting the role of low-frequency Atlantic variability in regulating inter-basin climate interactions. More broadly, this study emphasizes the importance of considering decadal background state when interpreting interannual climate relationships and improving seasonal-to-interannual climate prediction.

Supplementary Materials: The following supporting information can be downloaded at: https://www.mdpi.com/article/10.3390/atmos17090817/s1, Table S1: Seasonal phase-locking validation of IOD and ENSO in 30 CMIP6 models. Table S2: Lagged IOD–ENSO partial correlations under different AMO phases for CMIP6 models and their capability classification. Figure S1: Lagged partial regression of SST anomalies (shading, °C) and 925 hPa wind anomalies (vectors, m s^{-1}) onto the normalized SON (0) DMI in the LCG multi-model ensemble mean. (a–f) AMO positive phase; (g–l) AMO negative phase. The concurrent ENSO effect is removed by linearly regressing on the D (0) JF (+1) Niño 3.4 index. Dotted area indicates that the regressions are significant at 95% confidence level. Green boxes indicate the Atlantic Niño area; Figure S2: Lagged partial regression of the equatorial Walker circulation (10° S–5° N averaged) onto the normalized SON (0) DMI in the LCG multi-model ensemble mean. (a–f) AMO positive phase; (g–l) AMO negative phase. Shading denotes vertical velocity anomalies (Pa s^{-1}), and vectors represent the composite of zonal wind (u, m s^{-1}) and vertical velocity (ω, Pa s^{-1}), with ω multiplied by −100 for scaling. The concurrent ENSO signal is removed by linearly regressing on the D (0) JF (+1) Niño 3.4 index. Dotted area indicates that the regressions are significant at 95% confidence level; Figure S3: Lagged partial regression of sea surface height anomalies (shading, 10^{-2} m) onto the normalized SON (0) DMI in the LCG multi-model ensemble mean. (a–f) AMO positive phase; (g–l) AMO negative phase. The concurrent ENSO signal is removed by linearly regressing on the D (0) JF (+1) Niño 3.4 index. Dotted area indicates that the regressions are significant at 95% confidence level. Green boxes indicate the Atlantic Niño area.

Author Contributions: H.Z. and J.X. initiated the research. H.Z. wrote the manuscript. Y.Z., K.D. and J.X. helped revise the manuscript. Y.Z. provided CMIP6 data. All authors have read and agreed to the published version of the manuscript.

Funding: This research received no external funding.

Institutional Review Board Statement: Not applicable.

Informed Consent Statement: Not applicable.

Data Availability Statement: CMIP6 model data were obtained from the Earth System Grid Federation (ESGF) [https://aims2.llnl.gov/search/cmip6/, accessed on 18 June 2026]. ERSSTv5 are available from NOAA PSL [https://www.ncei.noaa.gov/products/extended-reconstructed-sst, accessed on 18 June 2026].

Acknowledgments: We acknowledge NOAA for providing ERSSTv4 data, and the modeling groups participating in CMIP6 for making their model outputs available. We thank the reviewers for their valuable comments.

Conflicts of Interest: The authors declare no conflicts of interest.

Abbreviations

The following abbreviations are used in this manuscript:

IOD	Indian Ocean Dipole
ENSO	El Niño-Southern Oscillation
CMIP6	Coupled Model Intercomparison Project Phase 6
AMO	Atlantic Multidecadal Oscillation
SST	Sea Surface Temperature
MME	Multi-Model Ensemble
DMI	Dipole Mode Index

References

1. Saji, N.H.; Goswami, B.N.; Vinayachandran, P.N.; Yamagata, T. A dipole mode in the tropical Indian Ocean. *Nature* **1999**, *401*, 360–363. [CrossRef] [PubMed]
2. Webster, P.J.; Moore, A.M.; Loschnigg, J.P.; Leben, R.R. Coupled ocean–atmosphere dynamics in the Indian Ocean during 1997–98. *Nature* **1999**, *401*, 356–360. [CrossRef] [PubMed]
3. McPhaden, M.J.; Zebiak, S.E.; Glantz, M.H. ENSO as an integrating concept in Earth science. *Science* **2006**, *314*, 1740–1745. [CrossRef] [PubMed]
4. Saji, N.; Yamagata, T. Possible impacts of Indian Ocean dipole mode events on global climate. *Clim. Res.* **2003**, *25*, 151–169. [CrossRef]
5. Li, X.; Yu, J.-Y.; Ding, R.; Xu, X.; Ji, K.; Wen, T. South Pacific oscillation contributes to multi-year ENSOs. *npj Clim. Atmos. Sci.* **2025**, *8*, 243. [CrossRef]
6. Annamalai, H.; Xie, S.P.; McCreary, J.P.; Murtugudde, R. Impact of Indian Ocean sea surface temperature on developing El Niño. *J. Clim.* **2005**, *18*, 302–318. [CrossRef]
7. Xie, S.-P.; Annamalai, H.; Schott, F.A.; McCreary, J.P. Structure and mechanisms of South Indian Ocean climate variability. *J. Clim.* **2002**, *15*, 864–878. [CrossRef]
8. Stuecker, M.F.; Timmermann, A.; Jin, F.; Chikamoto, Y.; Zhang, W.; Wittenberg, A.T.; Widiasih, E.; Zhao, S. Revisiting ENSO/Indian Ocean Dipole phase relationships. *Geophys. Res. Lett.* **2017**, *44*, 2481–2492. [CrossRef]
9. Wang, H.; Kumar, A.; Murtugudde, R.; Narapusetty, B.; Seip, K.L. Covariations between the Indian Ocean Dipole and ENSO: A Modeling Study. *Clim. Dyn.* **2019**, *53*, 5743–5761. [CrossRef]
10. Zhang, Y.; Li, J.; Xue, J.; Zheng, F.; Wu, R.; Ha, K.-J.; Feng, J. The relative roles of the South China Sea summer monsoon and ENSO in the Indian Ocean Dipole development. *Clim. Dyn.* **2019**, *53*, 6665–6680. [CrossRef]
11. Behera, S.K.; Luo, J.J.; Masson, S.; Rao, S.A.; Sakuma, H.; Yamagata, T. A CGCM Study on the interaction between IOD and ENSO. *J. Clim.* **2006**, *19*, 1688–1705. [CrossRef]
12. Izumo, T.; Vialard, J.; Lengaigne, M.; De Boyer Montegut, C.; Behera, S.K.; Luo, J.-J.; Cravatte, S.; Masson, S.; Yamagata, T. Influence of the state of the Indian Ocean Dipole on the following year's El Niño. *Nat. Geosci.* **2010**, *3*, 168–172. [CrossRef]
13. Fan, L.; Meng, X. The asymmetric predictive power of Indian Ocean dipole for subsequent year's ENSO: Role of the Atlantic Ocean as an intermediary. *Geophys. Res. Lett.* **2023**, *50*, e2023GL105525. [CrossRef]
14. Jin, Y.; Meng, X.; Zhang, L.; Zhao, Y.; Cai, W.; Wu, L. The Indian Ocean weakens the ENSO spring predictability barrier: Role of the Indian Ocean basin and dipole modes. *J. Clim.* **2023**, *36*, 8331–8345. [CrossRef]

15. Yuan, D.; Zhou, H.; Zhao, X. Interannual climate variability over the tropical Pacific Ocean induced by the Indian Ocean dipole through the Indonesian throughflow. *J. Clim.* **2013**, *26*, 7882–7896. [CrossRef]
16. Luo, J.-J.; Zhang, R.; Behera, S.K.; Masumoto, Y.; Jin, F.-F.; Lukas, R.; Yamagata, T. Interaction between El Niño and extreme Indian Ocean dipole. *J. Clim.* **2010**, *23*, 652–669. [CrossRef]
17. Wang, J.; Zhang, S.; Li, Y.; Sprintall, J. A Positive Indian Ocean Dipole Leads to an Indian Ocean Basin Mode That Favors the Development of La Niña the Following Year. *Geophys. Res. Lett.* **2025**, *52*, e2024GL112632. [CrossRef]
18. Yoo, J.-H.; Moon, S.; Ha, K.-J.; Yun, K.-S.; Lee, J.-Y. Cases for the sole effect of the Indian Ocean dipole in the rapid phase transition of the El Niño–Southern Oscillation. *Theor. Appl. Climatol.* **2020**, *141*, 999–1007. [CrossRef]
19. Clarke, A.J.; Liu, X. Interannual sea level in the northern and eastern Indian Ocean. *J. Phys. Oceanogr.* **1994**, *24*, 1224–1235. [CrossRef]
20. Sprintall, J.; Gordon, A.L.; Koch-Larrouy, A.; Lee, T.; Potemra, J.T.; Pujiana, K.; Wijffels, S.E. The Indonesian Seas and their role in the Coupled Ocean–Climate System. *Nat. Geosci.* **2014**, *7*, 487–492. [CrossRef]
21. Yuan, D.; Wang, J.; Xu, T.; Xu, P.; Hui, Z.; Zhao, X.; Luan, Y.; Zheng, W.; Yu, Y. Forcing of the Indian Ocean dipole on the interannual variations of the tropical Pacific Ocean: Roles of the Indonesian Throughflow. *J. Clim.* **2011**, *24*, 3593–3608. [CrossRef]
22. Zhou, Q.; Duan, W.; Mu, M.; Feng, R. Influence of positive and negative Indian Ocean dipoles on ENSO via the Indonesian throughflow: Results from sensitivity experiments. *Adv. Atmos. Sci.* **2015**, *32*, 783–793. [CrossRef]
23. Wang, H.; Jiao, M.; Huang, W.; Huang, L.; Zhang, S. Indonesian Throughflow variability under global warming in CMIP6 models. *J. Mar. Sci. Eng.* **2026**, *14*, 1059. [CrossRef]
24. Zhang, L.; Han, W. Indian Ocean dipole leads to Atlantic Niño. *Nat. Commun.* **2021**, *12*, 5952. [CrossRef] [PubMed]
25. Ding, H.; Keenlyside, N.S.; Latif, M. Impact of the equatorial Atlantic on the El Niño Southern Oscillation. *Clim. Dyn.* **2012**, *38*, 1965–1972. [CrossRef]
26. Izumo, T.; Lengaigne, M.; Vialard, J.; Luo, J.-J.; Yamagata, T.; Madec, G. Influence of Indian Ocean dipole and Pacific recharge on following year's El Niño: Interdecadal robustness. *Clim. Dyn.* **2014**, *42*, 291–310. [CrossRef]
27. Yuan, Y.; Li, C. Decadal variability of the IOD–ENSO relationship. *Sci. Bull.* **2008**, *53*, 1745–1752. [CrossRef]
28. Pillai, P.A.; Kiran, V.G.; Suneeth, K.V. The strengthened role of new predictors of Indian Ocean dipole (IOD) during the recent decades of weakened ENSO–IOD relationship. *Dyn. Atmos. Oceans* **2024**, *106*, 101432. [CrossRef]
29. Xue, J.; Luo, J.; Zhang, W.; Yamagata, T. ENSO–IOD inter-basin connection is controlled by the Atlantic multidecadal oscillation. *Geophys. Res. Lett.* **2022**, *49*, e2022GL101571. [CrossRef]
30. Ham, Y.-G.; Choi, J.-Y.; Kug, J.-S. The weakening of the ENSO–Indian Ocean dipole coupling strength in recent decades. *Clim. Dyn.* **2017**, *49*, 249–261. [CrossRef]
31. Xu, T.; Yuan, D.; Wang, J. Corrigendum: Assessment of the Oceanic Channel Dynamics Responsible for the IOD-ENSO Precursory Teleconnection in CMIP5 Climate Models. *Front. Clim.* **2022**, *4*, 1094092. [CrossRef]
32. Knight, J.R.; Folland, C.K.; Scaife, A.A. Climate impacts of the Atlantic Multidecadal Oscillation. *Geophys. Res. Lett.* **2006**, *33*, L17706. [CrossRef]
33. Li, X.; Xie, S.-P.; Gille, S.T.; Yoo, C. Atlantic-induced pan-tropical climate change over the past three decades. *Nat. Clim. Change* **2016**, *6*, 275–279. [CrossRef]
34. McGregor, S.; Timmermann, A.; Stuecker, M.F.; England, M.H.; Merrifield, M.; Jin, F.-F.; Chikamoto, Y. Recent Walker circulation strengthening and Pacific cooling amplified by Atlantic warming. *Nat. Clim. Change* **2014**, *4*, 888–892. [CrossRef]
35. Zhao, Y.; Capotondi, A. Interactions between tropical Atlantic and tropical Pacific in CMIP6 models. *J. Clim.* **2026**, *39*, 2097–2116. [CrossRef]
36. Wang, C. Three-Ocean Interactions and Climate Variability: A Review and Perspective. *Clim. Dyn.* **2019**, *53*, 5119–5136. [CrossRef]
37. Liu, T.; Song, X.; Tang, Y. The predictability study of the two flavors of ENSO in the CESM model from 1881 to 2017. *Clim. Dyn.* **2022**, *59*, 3343–3358. [CrossRef]
38. Huang, B.; Banzon, V.F.; Freeman, E.; Lawrimore, J.; Liu, W.; Peterson, T.C.; Smith, T.M.; Thorne, P.W.; Woodruff, S.D.; Zhang, H.-M. Extended Reconstructed Sea Surface Temperature Version 4 (ERSST.v4). Part I: Upgrades and Intercomparisons. *J. Clim.* **2015**, *28*, 911–930. [CrossRef]
39. Trenberth, K.E. The Definition of El Niño. *Bull. Am. Meteorol. Soc.* **1997**, *78*, 2771–2778. [CrossRef]
40. Bretherton, C.S.; Widmann, M.; Dymnikov, V.P.; Wallace, J.M.; Bladé, I. The effective number of spatial degrees of freedom of a time-varying field. *J. Clim.* **1999**, *12*, 1990–2009. [CrossRef]
41. Knight, J.R.; Allan, R.J.; Folland, C.K.; Vellinga, M.; Mann, M.E. A signature of persistent natural thermohaline circulation cycles in observed climate. *Geophys. Res. Lett.* **2005**, *32*, L20708. [CrossRef]
42. Zhang, R. Coherent surface-subsurface fingerprint of the Atlantic meridional overturning circulation. *Geophys. Res. Lett.* **2008**, *35*, L20705. [CrossRef]
43. Zhang, L.; Wang, C. Multidecadal North Atlantic sea surface temperature and Atlantic meridional overturning circulation variability in CMIP5 historical simulations. *J. Geophys. Res. Oceans* **2013**, *118*, 5772–5791. [CrossRef]

44. Yan, X.; Zhang, R.; Knutson, T.R. Underestimated AMOC variability and implications for AMV and predictability in CMIP models. *Geophys. Res. Lett.* **2018**, *45*, 4319–4328. [CrossRef]
45. Clement, A.; Bellomo, K.; Murphy, L.N.; Cane, M.A.; Mauritsen, T.; Rädel, G.; Stevens, B. The Atlantic Multidecadal Oscillation without a role for ocean circulation. *Science* **2015**, *350*, 320–324. [CrossRef] [PubMed]
46. Cane, M.A.; Clement, A.C.; Murphy, L.N.; Bellomo, K. Low-pass filtering, heat flux, and Atlantic multidecadal variability. *J. Clim.* **2017**, *30*, 7529–7553. [CrossRef]
47. Yamamoto, A.; Tatebe, H.; Nonaka, M. On the emergence of the Atlantic multidecadal SST signal: A key role of the mixed layer depth variability driven by North Atlantic Oscillation. *J. Clim.* **2020**, *33*, 3511–3531. [CrossRef]
48. Buckley, M.W.; Marshall, J. Observations, inferences, and mechanisms of the Atlantic Meridional Overturning Circulation: A review. *Rev. Geophys.* **2016**, *54*, 5–63. [CrossRef]
49. McKenna, S.; Santoso, A.; Gupta, A.S.; Taschetto, A.S.; Cai, W. Indian Ocean Dipole in CMIP5 and CMIP6: Characteristics, Biases, and Links to ENSO. *Sci. Rep.* **2020**, *10*, 11500. [CrossRef] [PubMed]
50. Chen, H.-C.; Jin, F.-F. Simulations of ENSO Phase-Locking in CMIP5 and CMIP6. *J. Clim.* **2021**, *34*, 5135–5149. [CrossRef]

Disclaimer/Publisher's Note: The statements, opinions and data contained in all publications are solely those of the individual author(s) and contributor(s) and not of MDPI and/or the editor(s). MDPI and/or the editor(s) disclaim responsibility for any injury to people or property resulting from any ideas, methods, instructions or products referred to in the content.